Observation of free oscillations after the 2010 Chile and 2011 Japan earthquakes by superconducting gravimeter in Kutch, Gujarat, India

Chandra Sekhar Pedapudi, Madhusudhana Rao Katlamudi, Séverine Rosat

Observation of Free Oscillations after the 2010 Chile and 2011 Japan earthquakes by Superconducting Gravimeter in Kutch, Gujarat, India

Chandra Sekhar Pedapudi[1, 2], Madhusudhanarao Katlamudi[1*] and Severine Rosat[3]

1: Institute of Seismological Research, Gandhinagar, Gujarat, India
2. Department of Earth Sciences, Gujarat University, Ahmedabad, Gujarat, India
3: Institut Terre et Environnement de Strasbourg, CNRS UMR 7063, Strasbourg, France

*Corresponding author: madhuspl@yahoo.com; ORCHID ID: 0000-0001-9216-9927

ABSTRACT

In this paper, we present observations of free oscillations of the Earth after major earthquakes in Chile (February 27, 2010, M_w 8.8) and Japan (April 11, 2011, M_w 9.1) using data from the dual-sphere superconducting gravimeter (SG - 055), installed at Badargadh (23°.47 N, 70°.62 E), Kutch, Gujarat, India in March 2009. To see the noise characteristics, we calculated the power spectral density of the gravity time series of 5 quiet days in the frequency band 0.05-20 mHz using the new low noise model (NLNM) as a reference. We compared the noise level of the Badargadh site to other SG sites around the world. This shows that the Badargadh SG is in a low noise state. We find that the noise increases at frequencies below 1 mHz. Such a characteristic is also observed in Djougou (Afrique, Benin) and Strasbourg (France). Using theoretical tides for Gujarat, we estimated a scale factor of about -814 nm/s^2/V for Grav1 (lower-sphere) and about -775 nm/s^2/V for Grav2 (upper-sphere). We corrected the influence of atmospheric pressure from the one-second gravity data before switching to the frequency domain. We extracted a total of 53 Earth's Free Oscillations (EFO) modes during the earthquake in Japan and about 47 EFO modes during the earthquake in Chile. We are clearly able to extract the lowest ${}_0S_2$ spheroidal mode (0.30945 mHz or 54 minutes) and ${}_0S_0$ radial mode (0.81439 mHz or 20 minutes).The longer time series shows individual ${}_0S_2$ singlets and ${}_0S_3$ (0.46855 mHz) singlets due to the Coriolis splitting effect. We cross-referenced the frequencies of these modes using the PREM model and previous global observations. The correlation coefficient between the observed and the PREM model for these two events are 0.999 for Japan earthquake and 0.993 for Chile earthquake. This validates the quality of the data useful for low frequency studies in seismology. We also calculated the relative deviations of our observed fundamental modes with previously determined observed and theoretical values. We found that the relative deviations of our observed free oscillations do not exceed 0.5%, indicating good correlations.

Keywords: Superconducting gravity data, Free Oscillations, PREM model

1. Introduction

In times of major earthquakes, volcanic eruptions or underground nuclear explosions, Earth free oscillations (EFO) are generated in addition to seismic waves such as body and surface waves [1]. Based on wave motion, free oscillations are mainly divided into two categories, namely spheroidal oscillations and toroidal oscillations [2]. In the case of spheroidal oscillations, the displacements are both radial and tangential, which can be described by the spherical harmonic functions. As for the toroidal oscillations, the displacements are purely tangential. In the past, the time series of very long period broadband seismographs were widely used to determine the frequency, phase and decay factor of various EFO [3]. Identification of EFO is also done using data of strainmeter and spring gravimeter [4]. Superconducting gravimeters (SGs) have the best precision and sensitivity compared to other instruments, making them excellent tools for characterizing the Earth's free oscillations [5, 6]. The SG can record normal modes between periods of 10 s to 54 minutes [7, 8]. SG is a type of instrument that can measure the vertical deformation of the Earth's surface and changes in the Earth's gravitational field over periods ranging from seconds to years, including normal modes, Earth tides and other phenomena, with a sampling rate of 1 or 2 seconds. SGs better characterize low-frequency seismic modes because their response to atmospheric pressure changes is linear at low frequencies and can be better reduced [9]. Benioff et al. [10] first identified the EFO mode using strain gauge data during the Kamchatka earthquake (M~9) in 1952, which is a spheroidal mode with a period of 57 minutes. Later, they found dozens of spheroidal free oscillations and toroidal modes using data from the 1960 Chilean earthquake. Besides large earthquakes, Tanimoto [11] and Nishida [12] report continuous free oscillations of the fundamental modes between frequencies of 0.3 and 5 mHz.

The deviations of the observed frequencies of the normal modes from their theoretical values are used to provide a measure of the deviation from the Earth's spherical symmetry including lateral heterogeneities, while the EFO attenuation provides a measure of internal inelasticity. In fact, seismic mode frequencies and damping factors were used to create the Preliminary Reference Earth Model (PREM), which is still widely used in seismology and beyond [13]. Observing the EFO gives us the opportunity to study the structure of the Earth's interior [14]. In the upper mantle, some modes are sensitive to compressional velocities while others in the lower mantle are sensitive to shear velocities [15, 16, 17]. By observing the EFO, we can also determine the magnitude, duration and amplitude of the earthquake that produces the EFO [18]. We can also

study the solutions of the focal mechanism of large earthquakes using the observed EFO [18, 19, 20].

Institute of Seismological Research has established the Multi-Parameter Geophysical Observatory at Badargadh (23.47°N, 70.62°E), Kutch, Gujarat, India to study earthquake precursors in an integrated manner. Eleven different types of parameters are monitored using instruments, namely Overhauser magnetometer, three-axis fluxgate magnetometer, induction coil magnetometer, DI Flux magnetometer, radon in soil monitor, radon in water, SG, water level recorder, differential GPS receiver, strong motion accelerometer and broadband seismometer. High-precision devices have the sensitivity to detect characteristic disturbances caused by tectonic activity near monitoring stations. The main objective of SG is to monitor the minute fluctuations (at the sub-microgal scale, where 1 μGal = 10 nm/s²) of the Earth's gravitational field due to small tectonic deformations and/or mass redistributions associated with the collision between Indian plate and Asian plate, and to study co-seismic/precursory gravitational signals, if any, to a large earthquake [22]. Arora et al. [23] reported the first observations of earth free oscillations during the April 1, 2007 Solomon Islands earthquake (MS=8.1) by Indian superconducting gravimeter in the Himalayan region. Two strong earthquakes have occurred in the last decade, namely the Tohoku earthquake of March 11, 2011 (Mw 9.1), which struck Japan (according to USGS data) with a focal depth of 29 km, and the earthquake in Chile on February 27, 2010 (Mw 8.8) with a focal depth of 23 km. The epicenters of earthquakes in Chile and Japan and the position of SG at Badargadh station are shown in Fig. 1. In this paper, we have examined all EFO modes of these two strong earthquakes using data recorded with a superconducting gravimeter in Badargadh, Gujarat, India and the observed free oscillations are compared with the PREM model [13].

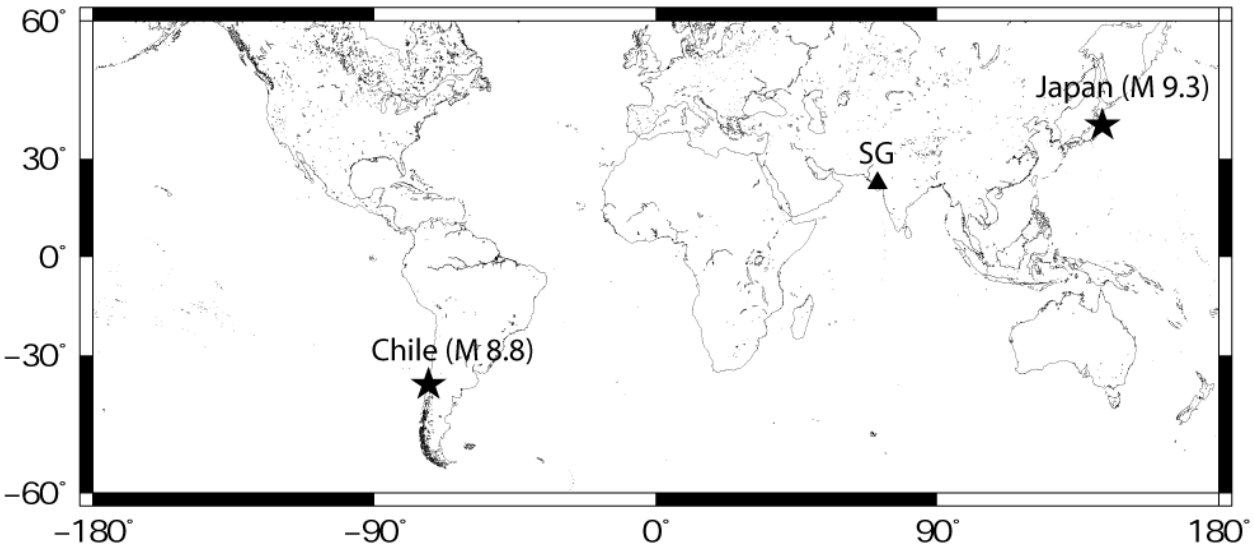

Figure 1: Location map of Both the Japan and Chile earthquakes Epicenters and the Super Conducting Gravimeter at Badargadh MPGO Station.

2. Data and Method

A superconducting gravimeter (SG) was installed in March 2009 in Badargadh, Gujarat, India and continuously records gravitational fluctuations at 1 sample/second (Hz). SGs are known to accurately measure the time-varying gravitational field with unprecedented resolution and temporal stability. Such an accurate and stable temporal gravity record gives us a unique opportunity to monitor and study a wide range of studies, from long-period tides to seismic normal modes [24]. By replacing the mechanical spring with the levitation of a magnetically suspended proof mass, the superconducting gravimeter solves the problem of erratic drift caused by relative gravimeters and seismometers in well-regulated environments [25]. The magnetic shield, the field coils and the levitating mass (sphere) are the three main superconducting elements of the SG [26]. The website (www.gwrinstruments.com) contains complete principles of operation for each of the elements of the superconducting gravimeter. The actual image of the superconducting gravimeter installed in Badargadh is shown in Fig2. The superconducting gravimeter we used is a two-sphere superconducting gravimeter, which increases data quality and has high consistency in drift tracking for better data resolution [27].

Figure 2: Superconducting Gravimeter placed in Badargadh station, Gujarat, India, a) DAC unit, b) Dewar and c) the dome structure

In our study, we collected gravitational data for two major earthquakes in Japan on March 11, 2011 and the Chile earthquake on February 27, 2010. For the identification of free oscillations, we used SG data spanning nearly 20 days (480 hours) after the occurrence of the respective earthquakes, and these data are subject to pre-processing using TSoft software [28] such as: removal of gravity tides, atmospheric pressure correction and spectral analysis of residual gravity data [29]. After removing the solid earth tides generated by the WDD model [30] from the raw data using TSoft, we then apply the 20-class fragmented polynomial fitting technique to remove the remaining gravitational tides. For the fragmental polynomial fit, the best transit time is about half a day. Using this technique, the gravitational tides are completely removed from the SG observational data, and now this remaining gravitational residual is subjected to the second step of the SG data preprocessing, which was the correction for the pressure effect. The pressure effect was corrected by multiplying the recorded barometric pressure variation P by a nominal

admittance of -3 nm/s^2/hPa [31]. After the pressure correction, we obtain the residual gravity time series, which are shown in Fig 3 for the Japan and Chile earthquakes.

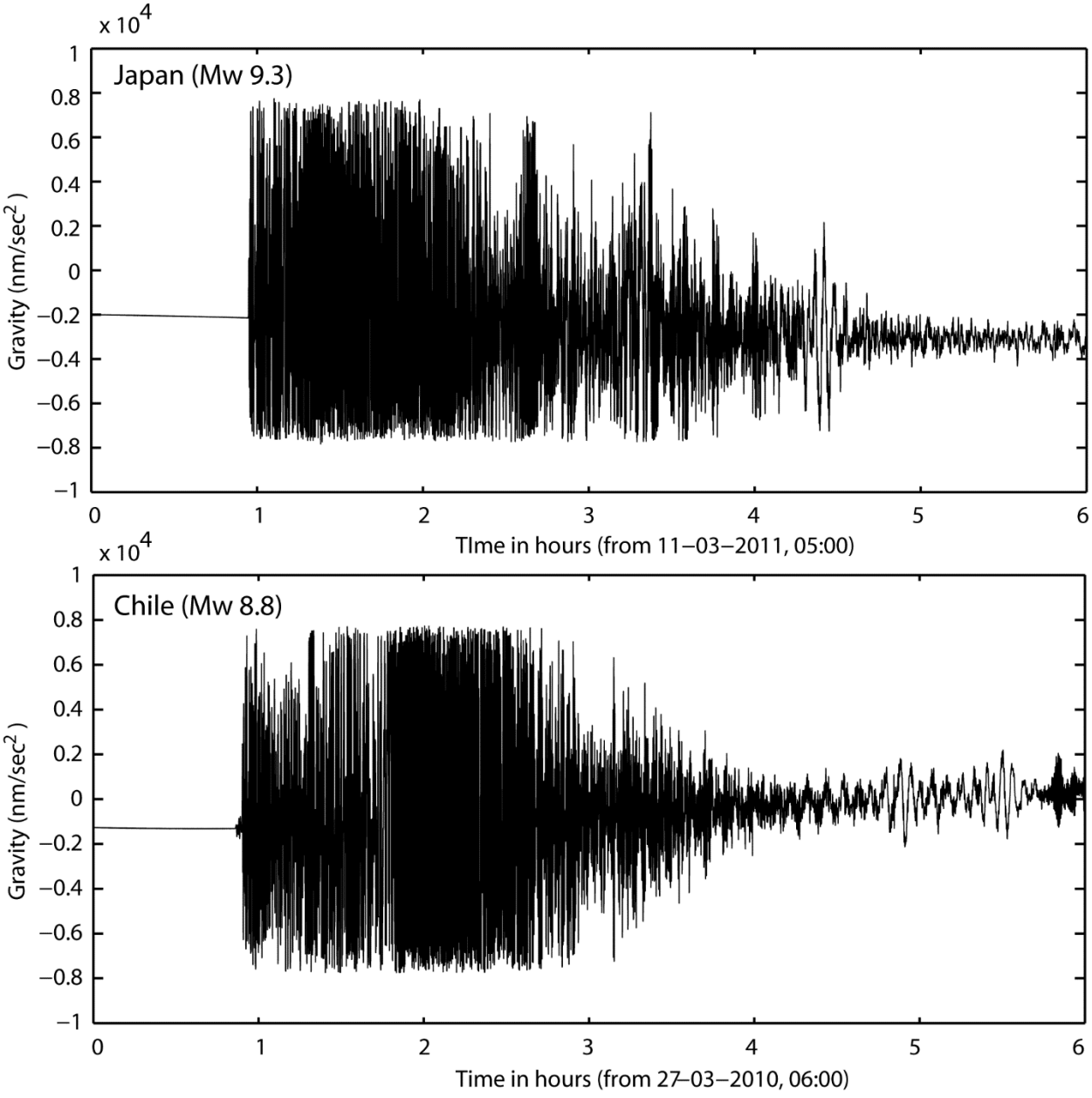

Figure 3: Gravity residuals during Japan and Chile earthquakes after the removal of gravity tides and pressure corrections

We now perform a spectral analysis of this residual gravity time series. Fast Fourier transform (FFT), wavelet analysis and maximum entropy spectrum are some of the methods reported in previous studies that can be used for spectral analysis. The maximum entropy spectrum is generally used for high frequency resolutions; however, it is only suitable for continuous signals.

Greater temporal resolution of observed signals is obtained with wavelet analysis, which is better suited for signals such as transients or damped oscillations. The FFT is best suited to signals such as harmonic signals because it has a high frequency resolution and can be used to detect free oscillations of the earth. Here, we apply the FFT technique to search for EFO signals in gravity residuals, and it is also effective in estimating signal-to-noise ratio of detected EFO modes. The EFO consists of an infinite number of decaying sinusoids. This decreasing nature introduces errors into the amplitude estimation by conventional Fourier analysis. To precisely identify the EFO, the local amplitude estimate of each sinusoid in each segment was obtained, and the attenuation in terms of quality factor Q was estimated from the amplitude variation of a frequency given in successive windows. A multi-radix FFT routine was used to calculate the Fourier transform, which does not require zero padding in the data. To further validate the identification of EFO modes, the observed frequencies of the modes are compared to the theoretical model based on different Earth models [21].

2.1 Noise Characteristics of Badargadh station

We are aware that SGs are renowned for their high sensitivity and low drift rates [8]. In order to assess their ability to provide useful information for seismology, it is important to determine their noise characteristics relative to other established instruments such as spring gravimeters and other SG sites. As part of the International Geodynamics and Earth tides Service (IGETS), around 18 superconducting gravimeters installed around the world have been connected. Since all installed SG stations are networked, it is possible to compare the noise levels of different SG stations. Understanding the noise levels at each location is essential for analyzing global earth processes. Banka and Crossley [29] initiated the study of noise characteristics near SG sites. Rosat et al. [32] developed a generalized method to study the noise characteristics at seismological frequencies. Rosat and Hinderer [33] further standardized the method to check the time stability of the noise characteristics of SG sites. To calculate noise characteristics at our SG site in Badargadh Gujarat, we used the method initially proposed Banka and Crossley [29] and generalized by Rosat and Hinderer [33].

We selected the five quietest days of the gravity time series based on their standard deviation [29] to determine the noise characteristics at the Badargadh site. The combined instrument and

site noises in the long period range are revealed by the power spectral density (PSD) spectrum of the five quietest days [29, 32, 34]. We calculated the power spectral densities for both sensors because the Badargadh has a dual sensor SG and the results are shown in Fig 4. The PSDs are compared with the NLNM [35] which is used as a seismological noise reference. As expected, the PSD becomes lower than the NLNM at frequencies below 1 mHz where the SG data have been corrected for tides and atmospheric pressure effect. The site noise PSD spectrum of Badargadh SG is observed with PSDs ranging from -220 dB to -140 dB. This shows that the SG at the Badargadh site falls below a low noise site with a seismic noise magnitude (SNM) of 1.13. We also compared the noise level of the Badargadh site to some other SG sites around the world. Noise increases sharply at frequencies below 1 mHz. Such a characteristic is also observed in Djougou (DJ, Benin) and Strasbourg (ST, France).

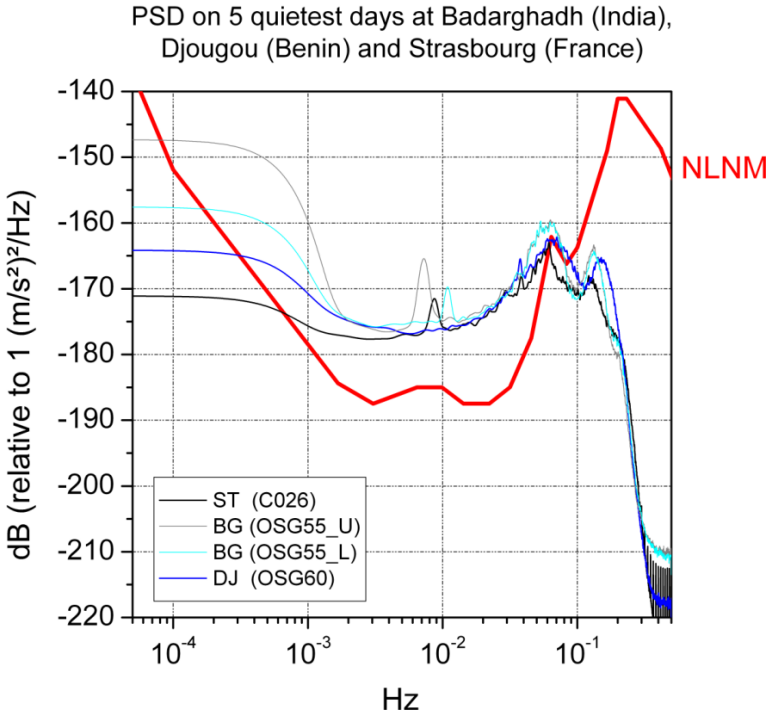

Figure 4: Comparison of SG near Badargadh with other SG sites from Djougou (DJ, Benin) and Strasbourg (ST, France). The new low noise model (NLNM) [35] is plotted as a reference.

In fact, the higher noise level observed at frequencies below 1 mHz must be the result of using the wrong scale factor resulting in an adequate tidal model used for the reduction of data. Using theoretical solid tides for Gujarat, we estimated a scale factor of about -814 nm/s^2/V for Grav1 and about -775 nm/s^2/V for Grav2. But it is a rough estimate as we used a solid earth tidal model whereas in Gujarat the ocean tides seem to be high. But using this estimated scale factor already

improves the low-frequency background noise. The spectral peak observed around 8-10 mHz for the 4 SGs is due to the resonance mode of the levitating sphere which has a slightly different period for each instrument.

2.2 Identification of Free oscillations of the earth for 2011 Japan and 2010 Chile earthquakes

The residual gravity time series generated after the tidal and atmospheric corrections were subjected to spectral analysis. If the instrument location has low ambient noise and we can use barometric data to reduce the atmospheric pressure contribution, normal modes can be very clearly identified using residual gravity data [36]. Since the ambient noise at the Badargadh site is extremely low and the atmospheric pressure is reduced, we can identify normal modes here. When the FFT is applied to the residual gravity time series after the Japan earthquake, which has a duration of nearly 249 hours after the event and a frequency resolution ratio (FRR) of nearly $1.1155*10^{-6}$ /sec, it shows the spectrum in the low frequency band up to 20 mHz. Fig 5 shows the spectrum up to 3 mHz, in which the gravest mode ($_0S_2$), breathing mode ($_0S_0$) and $_0S_3$ are clearly visible. The splitting of $_0S_2$ and $_0S_3$ due to Earth's rotation and ellipticity is illustrated by the presence of 4 and 3 spectral peaks respectively (Fig. 5). The Coriolis splitting is indeed dominant for modes below 1 mHz [36]. Please note that because of the source-receiver geometry, the singlet of $_0S_2$ corresponding to m = 0 is not visible at Gujarat station, while the 4 non-axial singlets are clearly visible. For $_0S_3$, only 3 singlets among the 7 are visible. Below 6 mHz, nearly 53 EFO modes were observed; of the 53 EFO modes, 47 represent the fundamental spheroid modes. These observed EFO modes are fitted to a synthetic Lorentzian resonance function to determine their frequency. We extract the error values for each mode as well as the frequency using the method described by Dahlen et al. (1982) [37]. All the observed EFO modes with their frequency and errors are listed in Table 1. We observed the frequency of 0.81468 mHz for $_0S_0$ mode instead of the 0.81465 mHz in the PREM model. Similarly, the gravest mode $_0S_2$ mode is observed with 0.3100 mHz (i.e. 53.76 minutes) instead of the 0.3092 mHz (i.e. 54 minutes) in the PREM model the PREM model.

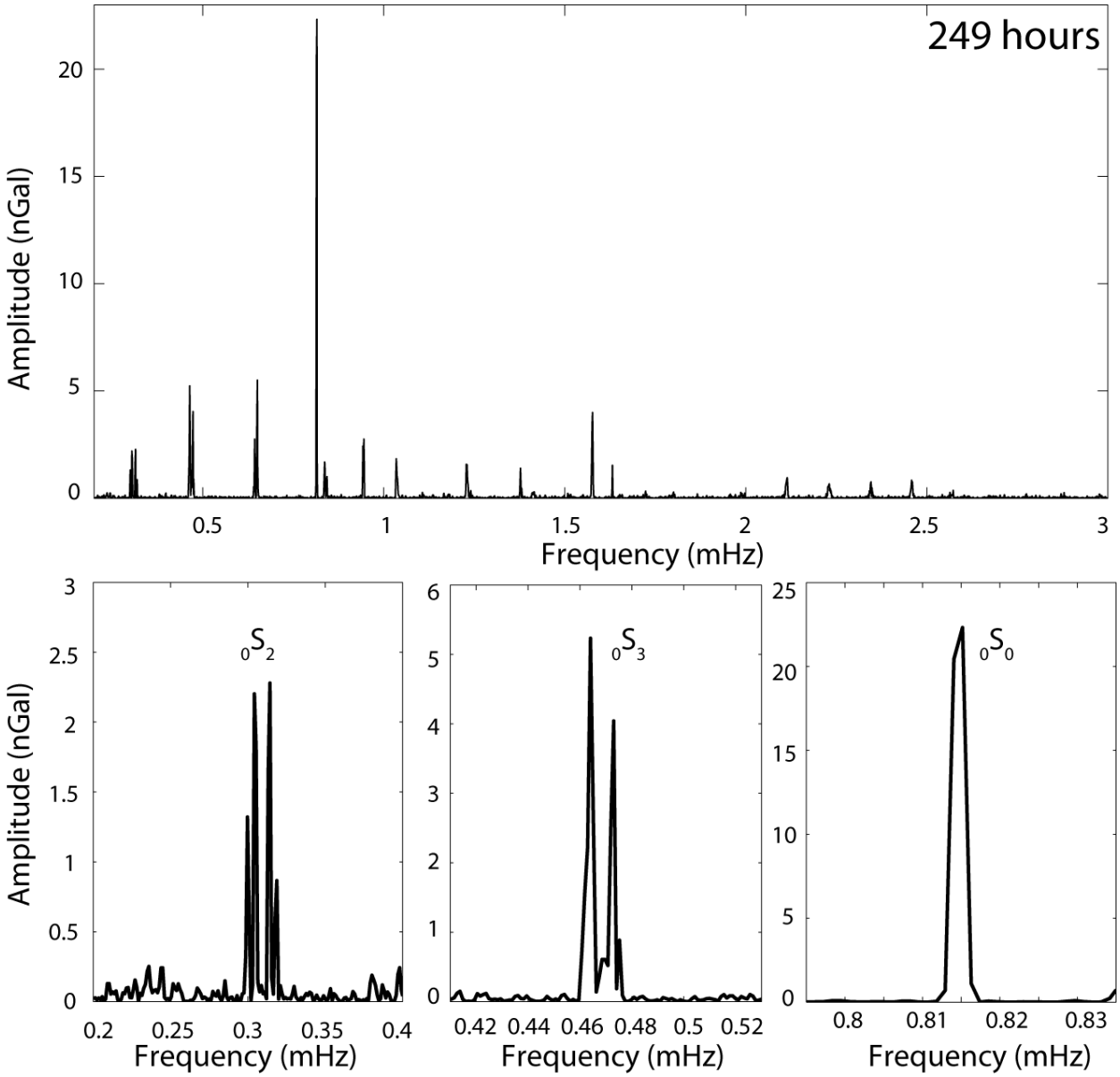

Figure 5: Spectrum of the Japan Earthquake after applying the FFT and the spectrum of the gravest mode ($_0S_2$), breathing mode ($_0S_0$) and the fundamental mode ($_0S_3$).

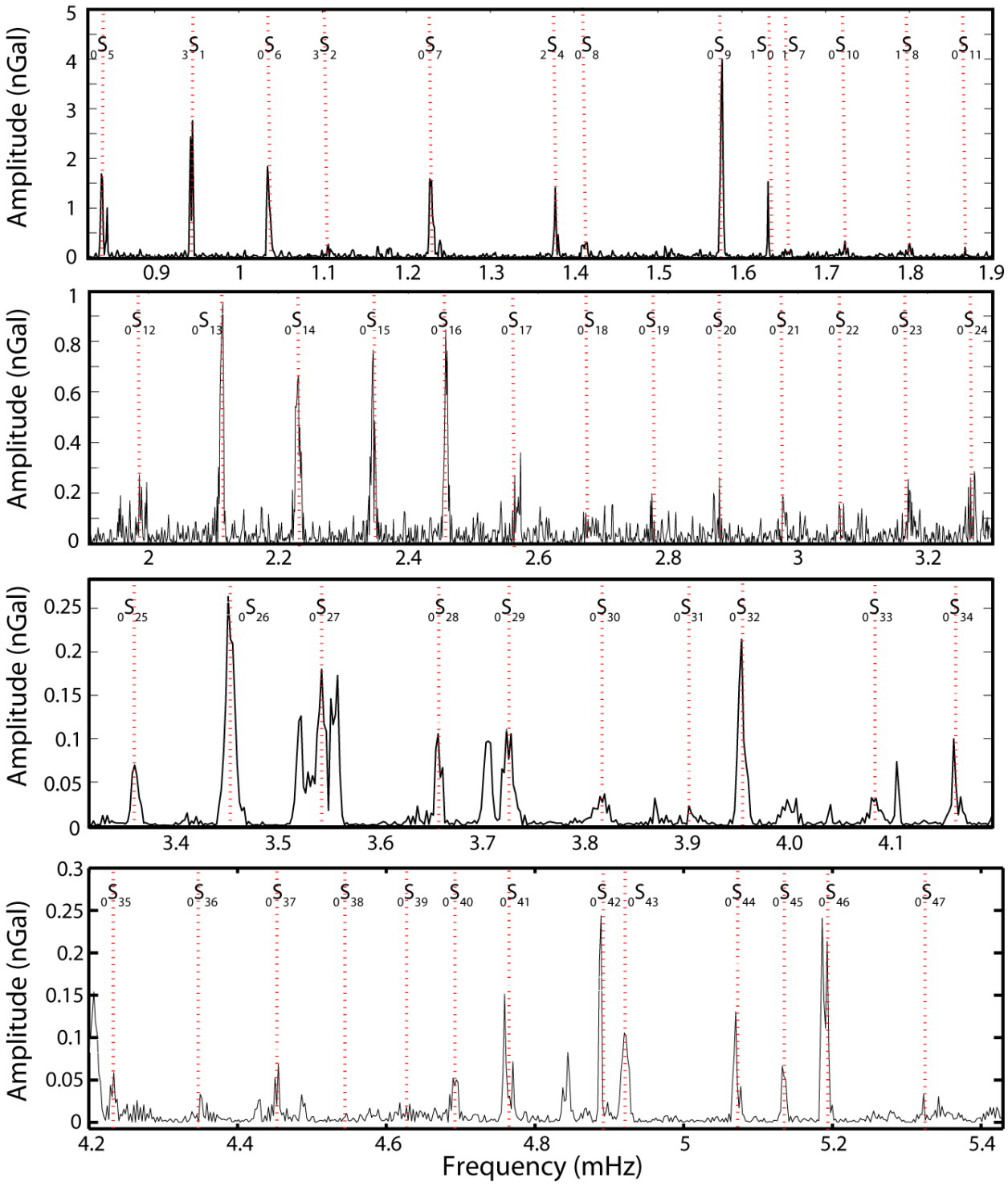

Figure 6: Observed spheroidal modes from ${}_0S_4$ to ${}_0S_{48}$ after Japan Earthquake. Used data length: 249 hours for modes ${}_0S_0$ to ${}_0S_{24}$ (top 2 panels); 120 hours for modes ${}_0S_{25}$ to ${}_0S_{47}$ (bottom 2 panels)

Fig 6 shows the amplitude-frequency spectra of all other EFO modes identified after the Japan earthquake. All of the EFO modes that have been observed have frequency ranges between 0.1

and 6 mHz. In addition to the 47 fundamental spheroidal modes, we were able to identify other EFO modes such as ${}_3S_1$, ${}_3S_2$, ${}_2S_4$, ${}_1S_0$, ${}_1S_7$ and ${}_1S_8$.

Table 1: Observed frequency and errors of EFO modes of Japan and Chile earthquakes

Mode	Observed Values (mHz)				Mode	Observed Values (mHz)			
	Japan		Chile			Japan		Chile	
	Frequency	Error	Frequency	Error		Frequency	Error	Frequency	Error
${}_0S_0$	0.81468	$\pm5.7\times10^{-9}$	0.81469	$\pm1.8\times10^{-8}$	${}_0S_{28}$	3.633	$\pm1.7\times10^{-10}$	3.6367	$\pm1.6\times10^{-10}$
${}_0S_2$	0.31006	$\pm3.1\times10^{-5}$	0.30961	$\pm1.1\times10^{-4}$	${}_0S_{29}$	3.7139	$\pm7.5\times10^{-12}$	3.7317	$\pm3.6\times10^{-11}$
${}_0S_3$	0.47072	$\pm4.9\times10^{-4}$	0.46943	$\pm2.5\times10^{-5}$	${}_0S_{30}$	3.8102	$\pm1.2\times10^{-10}$	3.8184	$\pm1.1\times10^{-7}$
${}_0S_4$	0.64949	$\pm2.2\times10^{-4}$	0.65021	$\pm4.1\times10^{-4}$	${}_0S_{31}$	3.9001	$\pm7.6\times10^{-11}$	3.9127	$\pm6.5\times10^{-11}$
${}_0S_5$	0.83951	$\pm5.1\times10^{-13}$	0.83557	$\pm7.1\times10^{-4}$	${}_0S_{32}$	3.993	$\pm1.1\times10^{-10}$	3.9975	$\pm4.9\times10^{-8}$
${}_0S_6$	1.0359	$\pm5.2\times10^{-9}$	1.0362	$\pm9.3\times10^{-6}$	${}_0S_{33}$	4.0854	$\pm7.8\times10^{-11}$	4.0804	$\pm4.5\times10^{-8}$
${}_0S_7$	1.2296	$\pm3.2\times10^{-9}$	1.2295	$\pm2.5\times10^{-9}$	${}_0S_{34}$	4.1784	$\pm6.1\times10^{-11}$	4.1827	$\pm2.9\times10^{-11}$
${}_0S_8$	1.4121	$\pm1.2\times10^{-8}$	1.4117	$\pm5.7\times10^{-9}$	${}_0S_{35}$	4.2645	$\pm7.3\times10^{-11}$	4.2342	$\pm9.1\times10^{-12}$
${}_0S_9$	1.576	$\pm3.5\times10^{-9}$	1.5753	$\pm1.4\times10^{-9}$	${}_0S_{36}$	4.3556	$\pm4.1\times10^{-11}$	4.3538	$\pm4.2\times10^{-11}$
${}_0S_{10}$	1.7231	$\pm1.1\times10^{-9}$	1.7232	$\pm9.1\times10^{-10}$	${}_0S_{37}$	4.4514	$\pm2.1\times10^{-11}$	4.4448	$\pm4.9\times10^{-4}$
${}_0S_{11}$	1.8562	$\pm1.7\times10^{-4}$	1.8568	$\pm6.6\times10^{-10}$	${}_0S_{38}$	4.5304	$\pm4.1\times10^{-11}$	4.5338	$\pm2.9\times10^{-7}$
${}_0S_{12}$	1.9872	$\pm4.8\times10^{-5}$	1.9885	$\pm2.4\times10^{-9}$	${}_0S_{39}$	4.6193	$\pm4.2\times10^{-11}$	4.6212	$\pm7.9\times10^{-10}$
${}_0S_{13}$	2.1127	$\pm3.5\times10^{-9}$	2.1104	$\pm4.5\times10^{-8}$	${}_0S_{40}$	4.7092	$\pm4.4\times10^{-11}$	4.713	$\pm1.8\times10^{-4}$
${}_0S_{14}$	2.2302	$\pm3.7\times10^{-9}$	2.2303	$\pm2.2\times10^{-9}$	${}_0S_{41}$	4.8002	$\pm3.6\times10^{-11}$	4.8237	$\pm6.2\times10^{-10}$
${}_0S_{15}$	2.3456	$\pm2.7\times10^{-9}$	2.3451	$\pm1.9\times10^{-9}$	${}_0S_{42}$	4.8795	$\pm2.4\times10^{-11}$	4.8977	$\pm1.1\times10^{-4}$
${}_0S_{16}$	2.4582	$\pm1.5\times10^{-9}$	2.4568	$\pm1.5\times10^{-9}$	${}_0S_{43}$	4.9712	$\pm2.6\times10^{-11}$	4.9864	$\pm1.8\times10^{-7}$
${}_0S_{17}$	2.5996	$\pm3.1\times10^{-10}$	2.566	$\pm9.1\times10^{-10}$	${}_0S_{44}$	5.0606	$\pm1.6\times10^{-11}$	5.0268	$\pm1.8\times10^{-4}$
${}_0S_{18}$	2.6658	$\pm1.1\times10^{-10}$	2.6719	$\pm9.6\times10^{-10}$	${}_0S_{45}$	5.1518	$\pm1.7\times10^{-11}$	-	-
${}_0S_{19}$	2.7792	$\pm6.6\times10^{-4}$	2.7753	$\pm6.9\times10^{-10}$	${}_0S_{46}$	5.241	$\pm1.7\times10^{-11}$	-	-
${}_0S_{20}$	2.8864	$\pm1.4\times10^{-5}$	2.8786	$\pm1.4\times10^{-10}$	${}_0S_{47}$	5.3306	$\pm1.4\times10^{-11}$	5.3373	$\pm5.1\times10^{-3}$
${}_0S_{21}$	2.98	$\pm1.9\times10^{-5}$	2.9781	$\pm3.1\times10^{-10}$	${}_3S_1$	0.94371	$\pm1.3\times10^{-8}$	-	-
${}_0S_{22}$	3.0713	$\pm2.8\times10^{-10}$	3.0739	$\pm2.7\times10^{-10}$	${}_3S_2$	1.1068	$\pm3.1\times10^{-10}$	-	-
${}_0S_{23}$	3.1689	$\pm4.6\times10^{-10}$	3.1707	$\pm1.5\times10^{-10}$	${}_2S_4$	1.3778	$\pm7.6\times10^{-9}$	-	-
${}_0S_{24}$	3.2715	$\pm2.2\times10^{-10}$	3.255	$\pm6.6\times10^{-11}$	${}_1S_0$	1.6315	$\pm4.4\times10^{-9}$	1.6223	$\pm1.2\times10^{-4}$
${}_0S_{25}$	3.3512	$\pm3.7\times10^{-11}$	3.364	$\pm2.7\times10^{-10}$	${}_1S_7$	1.6565	$\pm8.6\times10^{-9}$	-	-
${}_0S_{26}$	3.46	$\pm1.3\times10^{-3}$	3.4537	$\pm1.6\times10^{-10}$	${}_1S_8$	1.7987	$\pm2.2\times10^{-8}$	-	-
${}_0S_{27}$	3.5481	$\pm1.6\times10^{-10}$	3.5414	$\pm1.8\times10^{-10}$	${}_2S_8$	-	-	2.048	$\pm1.5\times10^{-3}$

Yan et al. (2016) [38] also found the spectral peaks of spheroidal modes between the frequency range of 1–4 mHz for the 2011 Japan earthquake. Compared to the PREM model, Cheng-Yin Chu et al. (2021) [39] found that all stimulated modes contain antinodes and that ${}_0S_9$–${}_0S_{43}$ spheroidal modes show prominent spectral peaks below 5 mHz. Above this frequency, however, it is difficult to observe EFO modes because the high frequency modes rapidly decay to the noise level due to the assumed long time, making them difficult to observe. We observed amplitude

ranges of 0 to 25 nGals for all modes for the Japan earthquake with a window length of 249 hours for modes ${}_0S_0$ to ${}_0S_{24}$ and 120 hours for the other modes. Similarly, we observed the amplitude range of 0 to 12 nGals for the Chile earthquake with a window length of 240 hours for the ${}_0S_0$ to ${}_0S_{24}$ modes and 120 hours for the other modes. We found that the amplitudes of the observed EFO modes decrease with increasing frequency, or in other words, the amplitude decreases with increasing time. Nishida and Kobayashi [40] also reported that above 5 mHz it is difficult to identify mode peaks because the constructive interference traveling wave is distorted due to heterogeneity and attenuation of the internal structure of the Earth.Kamal & Manisha et al. [5] obtained an amplitude range up to 40 nGal with a window length of almost 24 hours for the whole spectrum up to 5 mHz. For the identical 2011 Japan and 2010 Chile earthquakes, Zabranova et al. [41](2012) found that the amplitudes of EFO modes change drastically for different data lengths. In their study, the amplitude of the ${}_0S_0$ mode was determined to be 21.4 nGal for a data length of 250 hours and 18 nGal for a data length of 450 hours. This indicates that as the amount of data increases, the amplitude of the modes decreases. The results of our study with a data length of 240-249 hours are similar to those of Zabranova et al. [41] (2012) with a data length of 250 hours. For the Japan earthquake, we measured the amplitudes of ${}_0S_0$ is 22.32 nGal, ${}_0S_2$ is 2.279 nGal, and ${}_0S_3$ is 4.641 nGals. Similarly, for Chile earthquake, the amplitude value of ${}_0S_0$ is 11.45 nGal, ${}_0S_2$ is 10.15 nGal, and ${}_0S_3$ is 2.703 nGals. Rosat et al. [42] (2005) reported the amplitude of 8.4 nGal for the Peru earthquake (8.4 Mw) and 40 nGal for the Sumatra earthquake (9.3) with a data length of 240 hours. For the Japan earthquake after the ${}_0S_0$ mode, the ${}_0S_9$ mode has the second-highest amplitude value, which is 3.996 nGal. The amplitudes of high frequency modes below ${}_0S_{10}$, have shown identical values and a diminishing trend. Similarly in the case of Chile earthquake, the amplitudes of EFO modes up to ${}_0S_{35}$ are higher than the high frequency EFO modes that come after ${}_0S_{35}$. In comparison, the amplitudes of the EFO modes for the earthquake in Japan are higher than the amplitudes of the EFO modes for the earthquake in Chile. This conclusion can be related to the magnitude of the earthquake since the magnitude of the earthquake in Japan is greater than that of the earthquake in Chile.

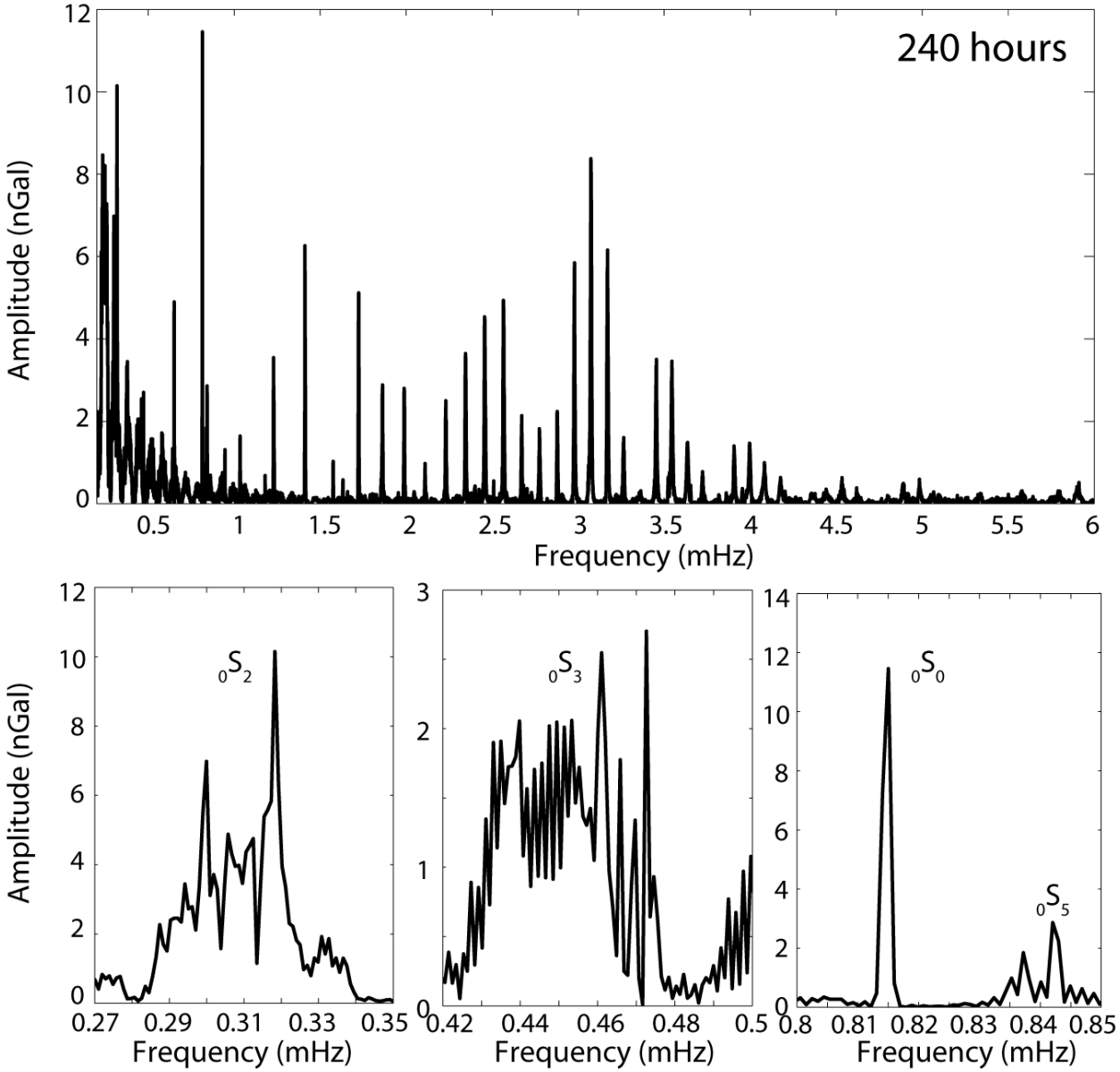

Figure 7: Spectrum of the FFT, gravest mode and the breathing mode after Chile Earthquake

Similarly, the EFO mode identification procedure is applied to the data of 2010 earthquake in Chile; we used the data length of almost 240 hours for this earthquake with a frequency resolution ratio (FRR) of $1.157 * 10^{-6}$ /sec. Again, we clearly identify 47 EFO modes, of which 45 are fundamental spherical modes, including gravest mode $_0S_2$ and the breathing mode $_0S_0$. The $_0S_0$ breathing mode was identified with a frequency of 0.81469 mHz for the Chile earthquake instead of the frequency of 0.81465 mHz in the PREM model, and likewise the 45 observed spheroidal nodes show reasonable agreement with the PREM model. The gravest mode $_0S_2$ mode must be observed with 0.3092 mHz (i.e. 54 minutes) according to the PREM model, while it

occurs at 0.3096 mHz (i.e. 53.83 minutes) as in our observations for the Chile earthquake. The individual $_0S_3$ singlets (0.46855 mHz) and $_0S_2$ singlets due to the Coriolis effect is also visible.

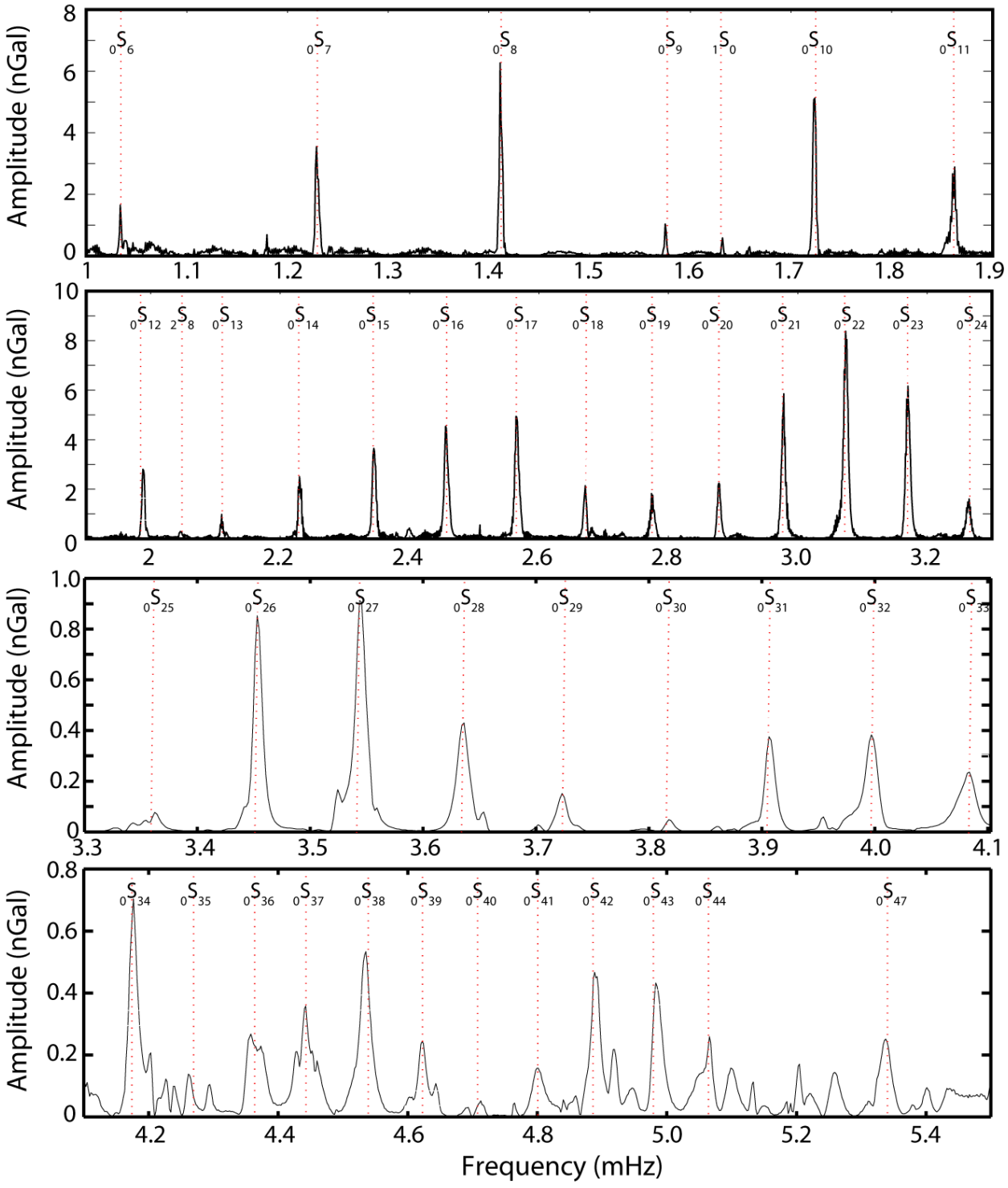

Figure 8: Observed spheroidal modes from $_0S_4$ to $_0S_{47}$ from Chile Earthquake. Used data length: 240 hours for modes $_0S_0$ to $_0S_{24}$ (top 2 panels); 120 hours for modes $_0S_{25}$ to $_0S_{47}$ (bottom 2 panels)

Fig. 7 shows the FFT amplitude spectrum of the Chile earthquake, along with its gravest modes ${}_0S_2$, ${}_0S_3$ and breathing mode ${}_0S_0$. Fig. 8 shows the amplitude-frequency spectra for all other EFO modes identified after the Chile earthquake. The observed EFO modes ranging from ${}_0S_6$ to ${}_0S_{47}$ are clearly visible in this figure, two of them ${}_0S_{45}$ and ${}_0S_{46}$ could not be identified. EFO modes such as ${}_1S_0$ and ${}_2S_8$ between these frequency ranges have also been identified. For this earthquake, we could only detect 47 fundamental modes below 6 mHz and could not locate clear spectral peaks above 6 mHz, while Wu Ye et al. (2013) [43] discovered about 76 different basic modes. We can also observe the amplitude ranges of these observed EFO modes, ranging from 0 to 12 nGal for all the EFO modes in frequency ranges from 0.1 to 6 mHz. Beyond this frequency, it becomes difficult to observe the EFO modes because the noise masks the modes as observed in the case of the earthquake in Japan.

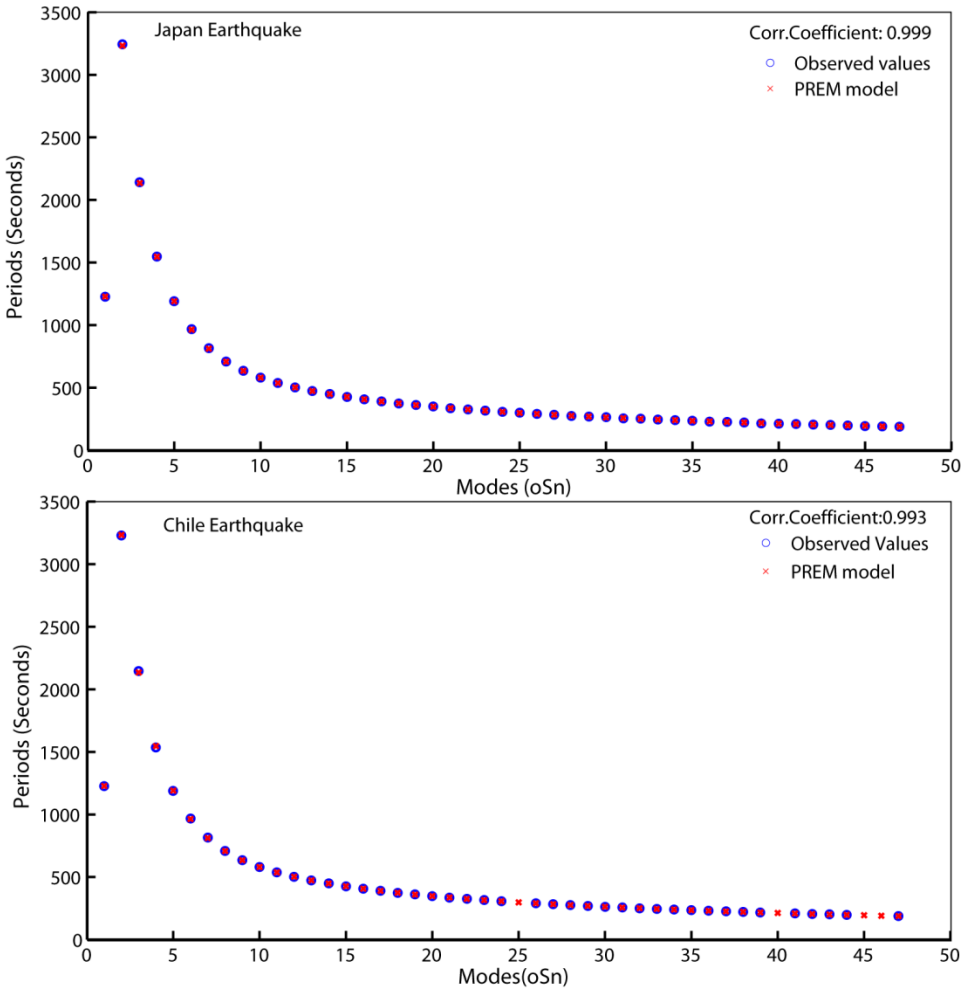

Figure 9: Correlation between the Japan Observed EFO periods (left panel); the Chile Observed EFO periods (right panel) and the theoretical PREM model periods

Arora et al. [23] first reported the observation of EFO using data from a superconducting gravimeter at Ghuttu, Uttarakhand in India. Later, Institute of Seismological Research installed the second superconducting gravimeter in Badargadh, Gujarat, India. We are the second to report the observation of EFO in India. Our observatory is located in western India while their observatory is located in northern India. Arora et al. [23] used data from the 2008 Solomon Islands earthquake (M 8.1) and reported almost 42 spheroidal modes. We were able to identify 47 EFO modes from the 2010 earthquake in Chile and 53 EFO modes from the 2011 earthquake in Japan. We obtained a correlation coefficient of 0.999 for Japan earthquake and 0.993 for Chile earthquake by comparing the observed frequencies with those predicted by the theoretical PREM model, indicating a strong correlation between the observed observations and the PREM observations. Fig. 9 illustrates the correlation between the periods observed in Japan; the periods observed in Chile and the periods of the PREM model. By comparing the amplitudes of the modes, we find that the amplitude of the ${}_0S_0$ mode of the Japan earthquake is 22.32 nGal, while the amplitude of the Chile earthquake is 11.46 nGal for the same ${}_0S_0$ mode. These EFO modes have different amplitudes but their frequencies are the same. If we look at the amplitudes of all EFO modes for earthquakes in Japan, the ${}_0S_9$ mode comes second with a measurement of 3.996 nGal. The amplitude values of all the other detected EFO modes are then almost identical for both the earthquakes. Until mode ${}_0S_{35}$, we find that the amplitudes of the EFO modes of the earthquake in Chile are comparable, but for higher-frequency modes, we find a decrease in their amplitudes. The measured EFO mode amplitudes of Japan earthquake are larger compared to the EFO mode amplitudes for the Chile earthquake. The amplitudes of these two earthquakes also showed a correlation, giving a correlation factor of 0.47%. It is possible to detect earthquakes at low frequencies without knowing them at high frequencies by comparing the spectral levels in small bands centered on the known frequencies of typical resonance peaks to the spectral levels of the background noise [44]. Thus, the unambiguous identification of normal low-frequency modes undoubtedly opens up new possibilities for studying low-frequency seismological research where conventional seismometers fail.

2.3 Comparison of the observed periods of EFO modes with the previous observations.

We applied the Fast Fourier Transform (FFT) technique to the Hanning-windowed residual gravity time series to obtain the frequency-amplitude spectra. Using the Lorentzian fitting, we obtain the frequency and error of all observed EFO modes. These frequency values are converted into periods. To identify EFO modes, these peak frequency values are compared to the theoretical frequencies of the EFO modes for the PREM model. In this section, we compare observed EFO mode periods to previously published observational and theoretical values. For this, we used results published in the study by Ness et al. [21]; Derr [45] and Dziewonski & Gilbert [46]. We have taken the theoretical periods of the spheroidal modes of Haddon and Bullen [47]; and Jordan and Anderson [48]. Table 2 contains a list of all the periods of observed EFO and other studies. We first calculated the relative variance of our observed periods with previously published observations and theoretical values to validate the results of our study. It uses the ratio of the difference between the theoretical and observed values to the observed values to calculate the relative deviation (RD). Fig. 10 shows the relative deviation of these observation periods after Japan and Chile earthquakes compared to the periods of the PREM model and to previous observations.

Table 2: Periods of observed EFO modes; previous results and theoretical values

Mode	Observed Periods (seconds)		PREM (S)	Ob_1 (s)	Ob_2 (s)	Ob_3 (s)	Th_1 (s)	Th_2 (s)
	Japan	Chile						
${}_0S_0$	1227.48	1227.46	1227.52	1227.7	1227.64	1227.64	1228.8	1227.61
${}_0S_2$	3225.18	3229.87	3234.15	3233.1	3233.3	3233.3	3226.9	3232.45
${}_0S_3$	2124.41	2130.24	2134.93	2139.2	2133.56	2133.56	2135.6	2134.13
${}_0S_4$	1539.67	1537.96	1545.83	1546	1547.16	1547.3	1547.2	1545.82
${}_0S_5$	1191.17	1196.79	1190.19	1188.4	1189.3	1190.12	1191.4	1190.42
${}_0S_6$	965.34	965.06	963.21	962.3	963.94	963.17	964.3	963.72
${}_0S_7$	813.27	813.34	811.49	809.1	811.67	811.45	812.5	812.24
${}_0S_8$	708.17	708.37	707.66	707.7	707.57	707.64	707.9	707.7
${}_0S_9$	634.52	634.80	633.91	634	634.01	633.95	633.9	633.69
${}_0S_{10}$	580.35	580.32	579.37	579.3	580.04	580.08	579.4	579.19
${}_0S_{11}$	538.74	538.56	536.91	536.8	536.46	536.56	537.1	536.87
${}_0S_{12}$	503.22	502.89	502.36	502.3	502.03	502.18	502.6	502.34
${}_0S_{13}$	473.33	473.84	473.17	473.2	473.05	473.14	473.5	473.21
${}_0S_{14}$	448.39	448.37	448.21	448.4	448.37	448.28	448.4	448.1
${}_0S_{15}$	426.33	426.42	426.17	426.3	426.19	426.24	426.4	426.16
${}_0S_{16}$	406.80	407.03	406.77	406.8	406.54	406.77	407	406.79
${}_0S_{17}$	384.67	389.71	389.41	389.3	389.37	389.31	389.7	389.56

${}_0S_{18}$	375.12	374.27	373.94	373.9	373.39	373.89	374.2	374.1
${}_0S_{19}$	359.82	360.32	360.15	361.5	360.57	360.2	360.1	360.14
${}_0S_{20}$	346.45	347.39	347.51	347.3	347.39	347.82	347.4	347.47
${}_0S_{21}$	335.57	335.78	335.82	335.8	335.8	336	335.8	335.88
${}_0S_{22}$	325.60	325.32	325.07	324.8	325.07	325.31	325.2	325.23
${}_0S_{23}$	315.57	315.39	315.31	315.5	315.11	315.43	315.3	315.38
${}_0S_{24}$	305.67	307.22	306.20	306.3	306.1	306.25	306.2	306.24
${}_0S_{25}$	298.40	297.26	297.67	297.6	297.54	297.71	297.7	297.72
${}_0S_{26}$	289.02	289.54	289.69	289.9	289.48	289.69	289.7	289.74
${}_0S_{27}$	281.84	282.37	282.21	281.8	282.38	282.34	282.3	282.25
${}_0S_{28}$	275.25	274.97	275.18	275.2	274.87	275.06	275.2	275.18
${}_0S_{29}$	269.26	267.97	268.46	268.4	268.27	268.44	268.5	268.49
${}_0S_{30}$	262.45	261.89	262.10	262.1	261.94	262.15	262.2	262.15
${}_0S_{31}$	256.40	255.58	256.02	256.2	256.02	256	256.2	256.12
${}_0S_{32}$	250.44	250.16	250.31	250.3	250.09	250.2	250.5	250.38
${}_0S_{33}$	244.77	245.07	244.88	245	245.3	244.95	245	244.91
${}_0S_{34}$	239.33	239.08	239.62	239.8	239.87	239.7	239.8	239.67
${}_0S_{35}$	234.49	236.17	234.60	234.9	234.51	234.69	234.8	234.66
${}_0S_{36}$	229.59	229.68	229.80	229.9	229.66	229.74	230	229.85
${}_0S_{37}$	224.65	224.98	225.17	224.9	224.75	225.16	225.4	225.24
${}_0S_{38}$	220.73	220.57	220.71	219.8	220.08	220.62	220.9	220.8
${}_0S_{39}$	216.48	216.39	216.45	216.4	216.45	216.43	216.6	216.54
${}_0S_{40}$	212.35	212.18	212.35	212.3	212.09	212.31	212.5	212.43
${}_0S_{41}$	208.32	207.31	208.33	208.3	207.88	208.05	208.5	208.47
${}_0S_{42}$	204.94	204.18	204.56	204.7	204.54	204.57	204.7	204.65
${}_0S_{43}$	201.16	200.55	200.90	200.8	201	200.93	200.9	200.96
${}_0S_{44}$	197.61	198.93	197.31	197.6	197.51	197.19	197.3	197.4
${}_0S_{45}$	194.11	-	193.91	194	193.91	194.03	193.9	193.95
${}_0S_{46}$	190.80	-	190.56	191.2	190.89	190.59	190.5	190.62
${}_0S_{47}$	187.60	187.36	187.33	187.4	187.48	187.43	187.2	187.4
${}_3S_1$	1059.65	-	1058.09	-	-	-	-	-
${}_3S_2$	903.51	-	904.32	-	-	-	-	-
${}_2S_4$	725.79	-	724.85	-	-	-	-	-
${}_1S_0$	612.93	616.41	613.01	-	-	-	-	-
${}_1S_7$	603.68	-	604.23	-	-	-	-	-
${}_1S_8$	555.95	-	556.02	-	-	-	-	-
${}_2S_8$	-	488.28	488.19	-	-	-	-	-

Obs_1=Ness et al. [21] Values, Obs_2= Derr [45] values, Obs_3= Dziewonski &Gilbert [46] values, Th_1= HB1 model [47], Th_2= Jordan and Anderson model [48].

We determined the relative deviation values of our observed spheroidal modes with the PREM model [13], Ness et al. [21](Obs_1), model HB1 [47](Th_1), we find that most modes have a relative deviation value less than or equal to 0.5%, with a few exceptions, some modes such as

$_0S_{32}$, $_0S_{36}$ and $_0S_{39}$ in the case of Japan earthquake. Most of the modes from $_0S_0$ to $_0S_{30}$ show more relative deviations, which can reach up to 0.1% compared to the other modes. In the case of the Chile earthquake, the modes $_0S_3$ & $_0S_4$ with the values of the PREM model [13] and the HB1 model [47] (Th_1), as well as $_0S_4$, $_0S_6$ & $_0S_7$ with Ness et al. [21] (Obs_1), the values show relative deviations of more than 0.5%.

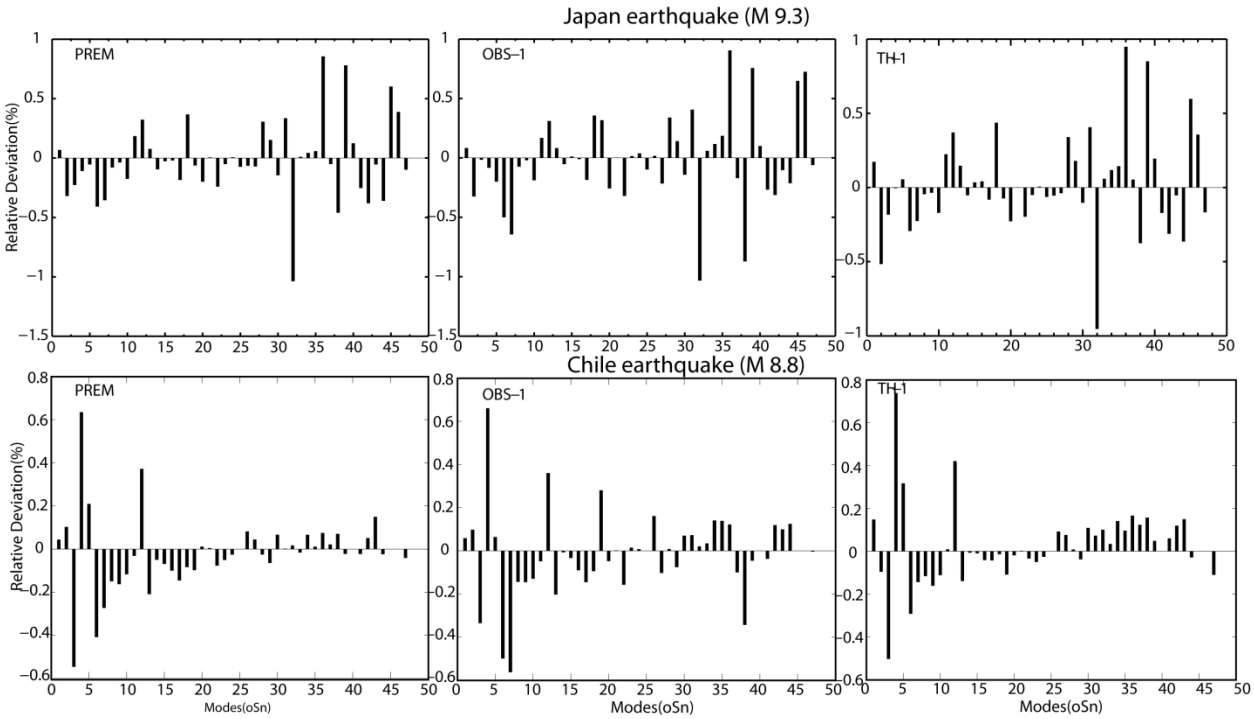

Figure 10: Relative Deviations of the observed periods with PREM model, Ness et al. [*20*] observations and the HB1 model [*47*]

Modes from $_0S_0$ to $_0S_{30}$ show a larger relative deviation from previous observations compared to modes from $_0S_{31}$ to $_0S_{43}$. We then subdivide the 47 spheroidal modes into 8 groups, each group containing 6 spheroidal modes, to further validate our observed results. Additionally, we calculate the mean relative deviation (ARD) for that specific range of normal modes, which is the average of the relative deviation values for each normal mode in a single RNM [47]. There are six different types of spheroid mode periods that we can use to calculate the relative deviation from our observed spheroidal mode periods. Therefore, there are six average relative deviations (ARD) for each normal mode range. Fig. 11 shows the ARDs for all RNMs for the Chile and Japan earthquakes.

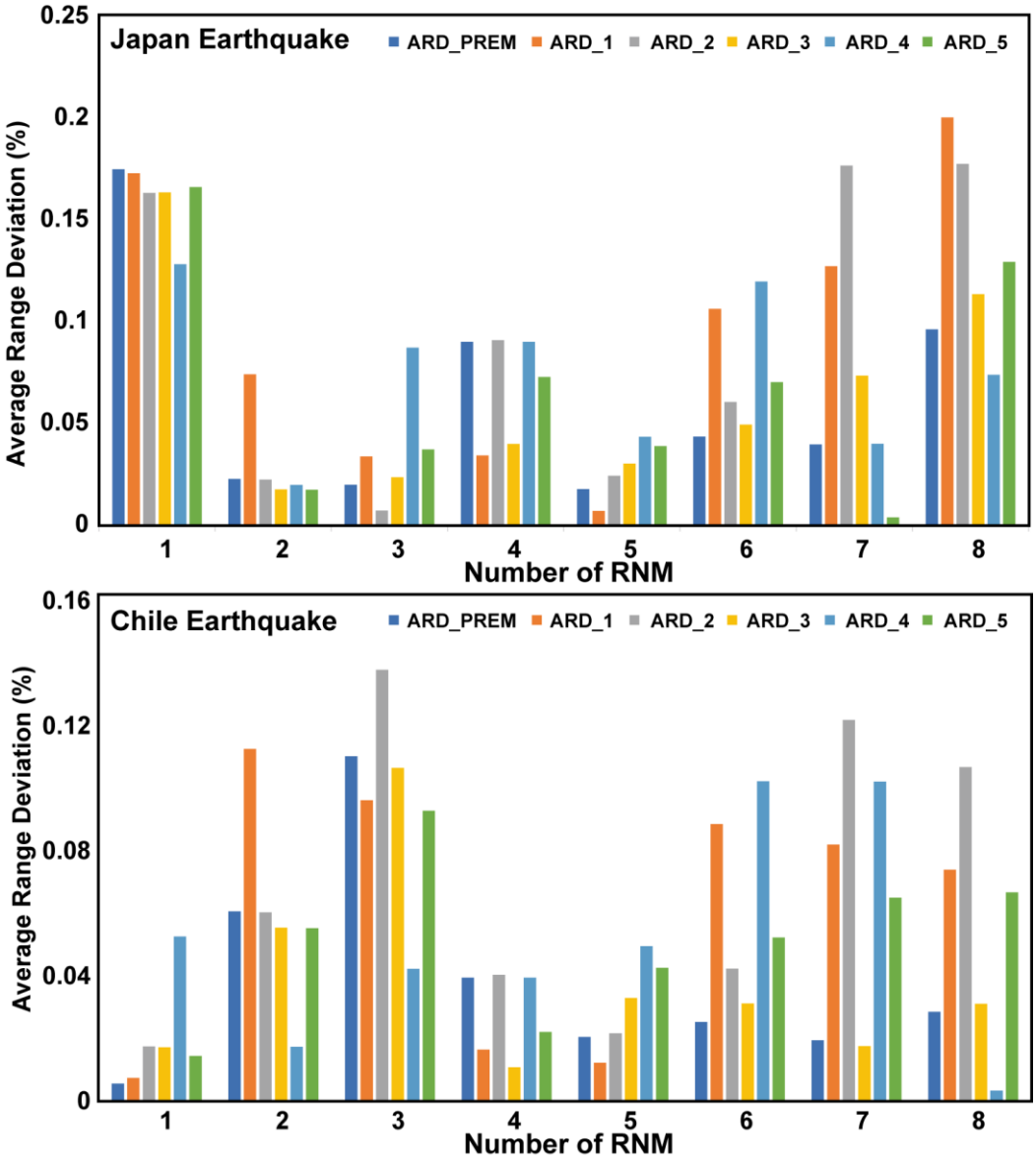

Figure 11: Average Relative Deviation of all the Range of Normal modes. ARD_1:Average Relative Deviation with Ness et al.,[21] observations, ARD_1: Average Relative Deviation with Deer [45] observations. ARD_3: Average Relative Deviation with Dziewonski &Gilbert [46] observations. ARD_4: Average Relative Deviation with HB1 model [47] observations, ARD_5: Average Relative Deviation with Jordan &Anderson model [48] observations and ARD_PREM: Average Relative Deviation with PREM model observations [13]

In connection with the observations of the Japan earthquake, we note that all of the 8 RNMs, except the first, have an average relative deviation (ARD) of 0.1%. The first RNM, on the other hand, has an ARD value of 0.18%. For RNMs 4 and 5, we noticed that only observations with Ness et al. [21] (ARD_1) & Derr [45](ARD_2) show a larger average relative deviation, which

has a value greater than 0.1%. As with the Chile earthquake, all RNMs except RNM 3 have ARD values less than or equal to 0.1%. In RNM 3, all observations have higher ARD values than other RNMs. We also note that in RNMs 3, 7 and 8, observations with Derr [45] (ARD_2) have ARD values greater than 0.1%. These results from the two earthquakes show that modes from $_0S_0$ to $_0S_{30}$ deviate more than the modes from $_0S_{31}$ to $_0S_{47}$. Lei et al. [49] reported that a larger relative deviation is found for $_0S_2$, $_0S_3$ spheroidal modes with the theoretical periods of these modes. Similarly, we find that modes from $_0S_0$ to $_0S_{30}$ exhibit larger relative deviations from previous observations and theoretical values.

3. Conclusions

In this paper, observations of free oscillations of the Earth are presented, obtained during two major earthquakes, the Japan and Chile earthquakes that occurred in 2011 and 2010, respectively. Based on comparisons of the noise characteristics of the Badargadh site with some other SG sites around the world, our SG site is classified as a low seismic noise site with a seismic noise magnitude (SNM) of 1.13 such as defined in Banka and Crossley (1999) [28]. We find that the noise increases at frequencies below 1 mHz. Such a characteristic is also observed in SG stations of Djougou (Benin, Africa) and Strasbourg (France). The scale factor for the two spheres of SG is calculated using theoretical solid tides and is -814 nm/s^2/V for Grav1 (lower sphere) and -775 nm/s^2/V for Grav2 (upper sphere). We were able to detect 53 EFO modes from the Japan earthquake and 47 EFO modes from the Chile earthquake using spectrum analysis, including breathing modes and gravest modes below 1 mHz. The frequencies of all these observed modes were correlated with predictions from the PREM model, giving a correlation factor of 0.999 for the Japan earthquake and 0.993 for the Chile earthquake, indicating that the resulting EFO modes are accurate. This validates the quality of the data useful for low frequency studies in seismology. The relative deviations of our observed EFO modes from previous observations show that the relative deviation does not exceed 0.5%, which means that our results correlate satisfactorily with previous studies.

Acknowledgement

The authors thank the Director General of the Institute of Seismological Research (ISR), Gandhinagar, for permission to carry out the work. The authors express their sincere gratitude to

the Department of Science and Technology, Government of Gujarat for providing the necessary funds for the study. The authors thank the organizers of the 19th International Symposium on Geodynamics and Earth Tides (G-ET 2021) on June 22-23, 2021. The authors thank two anonymous reviewers and Dr. Yiyan Zhou, Editor-in-Chief, Geodesy and Geodynamics, for their constructive comments which greatly improved the manuscript.

4. References

1 Buland, Ray. "Free oscillations of the Earth." *Annual Review of Earth and Planetary Sciences* 9 (1981): 385-413.

2 Dahlen, FAand, and Jeroen Tromp. "Theoretical global seismology." *Theoretical Global Seismology*. Princeton university press, (1998).

3 Masters, Guy, and Freeman Gilbert. "Structure of the inner core inferred from observations of its spheroidal shear modes." *Geophysical Research Letters* 8.6 (1981): 569-571.

4 Zürn, W., A.M.G. Ferreira, R. Widmer-Schnidrig, K. Lentas, L. Rivera, E. Clévédé, High-quality lowest-frequency normal mode strain observations at the Black Forest Observatory (SW-Germany) and comparison with horizontal broad-band seismometer data and synthetics, *Geophysical Journal International*, Volume 203, Issue 3, December (2015), Pages 1787–1803, https://doi.org/10.1093/gji/ggv381

5 Kamal and Mansinha, L.:, A test of the superconducting gravimeter as a long-period seismometer, *Phys. Earth Planet. Int*. (1992) 71, 52–60.

6 Zürn, W., and H-G. Wenzel. "High quality data from La Coste-Romberg gravimeters with electrostatic feedback: A challenge for superconducting gravimeters." *Marées terrestres (Bruxelles)* 110 (1991): 7940-7952.

7 Crossley, D., et al. "Network of superconducting gravimeters benefits a number of disciplines." *Eos, Transactions American Geophysical Union* 80.11 (1999): 121-126. 10.1029/99EO00079

8 Van Camp, M. "Measuring seismic normal modes with the GWR C021 superconducting gravimeter." *Physics of the Earth and Planetary Interiors* 116.1-4 (1999): 81-92.

9 Zürn, W., and R. Widmer. "On noise reduction in vertical seismic records below 2 mHz using local barometric pressure." *Geophysical Research Letters* 22.24 (1995): 3537-3540.

10 Benioff, Hugo, Frank Press, and Stewart Smith. "Excitation of the free oscillations of the Earth by earthquakes." *Journal of Geophysical Research* 66.2 (1961): 605-619.

11 Tanimoto, Toshiro. "Continuous free oscillations: atmosphere-solid earth coupling." *Annual Review of Earth and Planetary Sciences* 29.1 (2001): 563-584.

12 Nishida, Kiwamu. "Earth's background free oscillations." *Annual Review of Earth and Planetary Sciences* 41 (2013): 719-740.

13 Dziewonski, Adam M., and Don L. Anderson. "Preliminary reference Earth model." *Physics of the earth and planetary interiors* 25.4 (1981): 297-356.

14 Smith, Stewart Wilson. *An investigation of the earth's free oscillations*. Diss. California Institute of Technology, (1961).

15 Lowrie, William, and Andreas Fichtner. *Fundamentals of geophysics*. Cambridge university press, 2020.

16 He, Xiong, and Jeroen Tromp. "Normal- mode constraints on the structure of the Earth." *Journal of Geophysical Research: Solid Earth* 101.B9 (1996): 20053-20082.

17 Giardini, Domenico, Xiang- Dong Li, and John H. Woodhouse. "Splitting functions of long- period normal modes of the Earth." *Journal of Geophysical Research: Solid Earth* 93.B11 (1988): 13716-13742.
18 Park, Jeffrey, et al. "Earth's free oscillations excited by the 26 December 2004 Sumatra-Andaman earthquake." *Science* 308.5725 (2005): 1139-1144.
19 Jiang, Ying, et al. "Constraining the focal mechanism of the Lushan earthquake with observations of the Earth's free oscillations." *Science China Earth Sciences* 57.9 (2014): 2064-2070.
20 Zábranová, E., et al. "Constraints on the centroid moment tensors of the 2010 Maule and 2011 Tohoku earthquakes from radial modes." *Geophysical research letters* 39.18 (2012).
21 Ness, N. F., J. C. Harrison, and L. B. Slichter. "Observations of the free oscillations of the earth." *Journal of Geophysical Research* 66.2 (1961): 621-629.
22 Imanishi, Yuichi, et al. "A network of superconducting gravimeters detects submicrogal coseismic gravity changes." *Science* 306.5695 (2004): 476-478.
23 Arora, B. R., et al. "First observations of free oscillations of the earth from Indian superconducting gravimeter in Himalaya." *Current Science* (2008): 1611-1617.
24 Richter, B., et al. "From Chandler wobble to free oscillations: comparison of cryogenic gravimeters and other instruments in a wide period range." *Physics of the Earth and Planetary Interiors* 91.1-3 (1995): 131-148.
25 Prothero Jr, W. A., and J. M. Goodkind. "A superconducting gravimeter." *Review of Scientific Instruments* 39.9 (1968): 1257-1262.
26 Goodkind, John M. "The superconducting gravimeter." *Review of scientific instruments* 70.11 (1999): 4131-4152.
27 Harnisch, M., et al. The dual sphere superconducting gravimeter GWR. Geodesy Beyond 2000: The Challenges of the First Decade, IAG General Assembly Birmingham, July 19–30, 1999 *121* (2000): 155
28 Van Camp, M., and Vauterin, P., "Tsoft: graphical and interactive software for the analysis of time series and Earth tides" *Computers & Geosciences*, 31(5), (2005) 631-640, doi: 10.1016/j.cageo.2004.11.015,.
29 Banka, Dirk, and David Crossley. "Noise levels of superconducting gravimeters at seismic frequencies." *Geophysical Journal International* 139.1 (1999): 87-97.
30 Dehant, V., Defraigne, P., Wahr, J., Tides for a convective earth. *J. Geophys. Res*. 104 (B1), (1999) 1035–1058.
31 Merriam, J.B., Atmospheric pressure and gravity. Geophys. J. Int. 109 (3), (1992) 488–500.
32 Rosat, S., J. Hinderer, D. Crossley, and J. P. Boy, Performance of superconducting gravimeters from long-period seismology to tides, *J. Geodyn*., 38(3 - 5), (2004) 461– 476..
33 Rosat, Séverine, and Jacques Hinderer. "Noise levels of superconducting gravimeters: updated comparison and time stability." *Bulletin of the Seismological Society of America* 101.3 (2011): 1233-1241.
34 Riccardi, U., Séverine Rosat, and Jacques Hinderer. "Comparison of the Micro-g LaCoste gPhone-054 spring gravimeter and the GWR-C026 superconducting gravimeter in Strasbourg (France) using a 300-day time series." *Metrologia* 48.1 (2011): 28.
35 Peterson, Jon R. *Observations and modeling of seismic background noise*. No. 93-322. US Geological Survey, (1993).
36 Widmer-Schnidrig, R. "What can superconducting gravimeters contribute to normal-mode seismology?." *Bulletin of the Seismological society of America* 93.3 (2003): 1370-1380.
37 Dahlen, F. A. "The effect of data windows on the estimation of free oscillation parameters." *Geophysical Journal International* 69.2 (1982): 537-549.

38 Yan, Rui, et al. "Earth's free oscillations excited by the 2011 Tohoku M w 9.0 earthquake detected with a groundwater level array in mainland China." *Geophysical Journal International* 206.3 (2016): 1457-1466.

39 Cheng-Yin, Chu, et al. "Earth's free oscillations excited by the 2011 Tohoku earthquake recorded in multiple GPS networks." *Earth, Planets and Space (Online)* 73.1 (2021).

40 Nishida, Kiwamu, and Naoki Kobayashi. "Statistical features of Earth's continuous free oscillations." *Journal of Geophysical Research: Solid Earth* 104.B12 (1999): 28741-28750.

41 E. Zabranova, C. Matyska, L. Hanyk, and V. Palinkas. Constraints on the centroid moment tensors of the 2010 maule and 2011 tohoku earthquakes from radial modes. *Geophysical Research Letters*, 39, Sep 21 (2012). doi:10.1029/2012GL052850

42 S. Rosat, T. Sato, Y. Imanishi, J. Hinderer, Y. Tamura, H. McQueen, and M. Ohashi. High resolution analysis of the gravest seismic normal modes after the 2004 mw=9 Sumatra earthquake using superconducting gravimeter data. *Geophysical Research Letters*, 32(13), JUL 2005. doi:10.1029/2005GL023128.

43 Wu, Ye, Shu Yang, and Liang Ding. "The Earth's Free Spherical Oscillations of the Chile Earthquake." *Advanced Materials Research*. Vol. 622. Trans Tech Publications Ltd, 2013.

44 Beroza, Gregory C., and Thomas H. Jordan. "Searching for slow and silent earthquakes using free oscillations." *Journal of Geophysical Research: Solid Earth* 95.B3 (1990): 2485-2510.

45 Derr, John S. "Internal structure of the earth inferred from free oscillations." *Journal of Geophysical Research* 74.22 (1969): 5202-5220.

46 Dziewonski, A. M., and Freeman Gilbert. "Observations of normal modes from 84 recordings of the Alaskan earthquake of 1964 March 28." *Geophysical Journal International* 27.4 (1972): 393-446.

47 Haddon, R. A. W., and K. E. Bullen. "An earth model incorporating free earth oscillation data." *Physics of the Earth and Planetary Interiors* 2.1 (1969): 35-49.

48 Jordan, Thomas H., and Don L. Anderson. "Earth structure from free oscillations and travel times." *Geophysical Journal International* 36.2 (1974): 411-459.

49 Lei, Xiang'E., Houze Xu, and Heping Sun. "Detection of spheriodal free oscillation excited by Peru 8.2 M s earthquake with five international superconducting gravimeter data." *Science in China Series D: Earth Sciences* 48.1 (2005): 123-133.